

# Spatial frequency domain Mueller matrix imaging

Joseph Chue-Sang,<sup>1,2\*</sup> Aaron M. Goldfain,<sup>2,3</sup> Jeeseong Hwang,<sup>3</sup> and Thomas A. Germer<sup>2</sup>

<sup>1</sup>Department of Chemistry and Biochemistry  
University of Maryland  
College Park, MD 20742

<sup>2</sup>Sensor Science Division  
National Institute of Standards of Technology  
100 Bureau Dr., Gaithersburg, MD 20899

<sup>3</sup>Applied Physics Division  
National Institute of Standards of Technology  
325 Broadway, Boulder, CO 80305

We combine Mueller matrix polarimetry (MMP) with spatial frequency domain imaging (SFDI) to create a technique that is sensitive to near-surface material anisotropy. We demonstrate this imaging modality with scattering and absorbing phantoms and with a fiber optic bundle. Images of depolarization show reduced depolarization under high spatial frequency illumination and demodulation and in some cases, reduced contrast to deeper features. The images of a fiber optic bundle show marked differences between illumination modulations that are aligned with the fibers versus those crossed with the fibers, demonstrating the impact of polarization on scattering direction.

Keywords: anisotropy; Mueller matrix; polarimetry; scattering; spatial frequency imaging

## 1 Introduction

The Mueller matrix fully characterizes the polarization-sensitive reflection or transmission properties of a material for a given pair of incident and emitted directions.<sup>1,2</sup> From the Mueller matrix specific polarimetric properties, such as retardance, diattenuation, and depolarization, can be determined. Highly scattering materials, such as biological tissues and optical phantoms intended to mimic them, generally exhibit a strong depolarizing response.<sup>3</sup> Retardance and diattenuation can be observed in anisotropic media, such as connective tissue and muscle. Changes in retardance and diattenuation can reflect disruptions in connective tissue, and Mueller matrix polarimetry (MMP) has been shown to be useful for detecting changes in connective tissue, such as in cervixes during pregnancy or cancer.<sup>4,5</sup> Circular diattenuation has been observed in materials containing chiral molecules, such as <sup>4,5</sup> Circular diattenuation has been observed in materials containing chiral molecules, such as light-harvesting bacteria and leaves.<sup>6-8</sup> MMP is commonly conducted using full field illumination, allowing it to characterize a large sample region. The measured Mueller matrix results from all the paths the light takes, including those that have penetrated deeply into the sample. Biological tissues, however, are rarely uniform in their optical properties throughout a volume and discriminating the contributions from surface and deep tissues can be important. Organization of structures, such as cell nuclei, organelles, and other proteins, is important in distinguishing healthy and diseased tissue, and MMP is particularly sensitive to changes in structure organization. One issue with MMP is that deeply penetrating photons can impede detection of those photons that have only interacted with shallow tissues. Confocal MMP imaging has been one technique that has been used to circumvent this issue.<sup>9</sup>

Spatial frequency domain imaging (SFDI) has the potential for controlling the penetration depth of investigating photons.<sup>10,11</sup> In SFDI, a sinusoidal pattern is projected onto the material and the amplitude of the modulations is recorded as the phase of that pattern is varied. In this manner, only photon paths whose lengths are shorter than the period of the pattern are sensed, making depth sensitivity possible. A high spatial frequency can mitigate the effect of

---

\*Author to whom correspondence should be addressed: joseph.chue-sang@nist.gov

absorption by decreasing the amount of multiply-scattered photons detected in favor of singly scattered photons and providing better image contrast.<sup>10,12</sup> Because the sinusoidal pattern is projected on the sample, SFDI provides full field imaging, allowing for a macroscopic sample area to be investigated.

In this paper, we describe the combination of SFDI and MMP imaging and present some example measurements. Combining SFDI with MMP is relatively straightforward as only one extra step that is already compatible with the polarization state generator (PSG), must be added. Both modalities are also inexpensive compared to some imaging modalities, such as confocal imaging or optical coherence tomography. By combining these methods, we hope to combine the structural sensitivity of MMP with the photon path length selectivity of SFDI. This work expands a previous study,<sup>13</sup> which first explored this combination of modalities, by improving upon the data acquisition and expanding the range of materials studied.

## 2 Methods

### 2.1 Instrumentation

Figure 1(a) shows an illustration of the system. Structured illumination is generated using a digital light processing (DLP) projector (Texas Instruments, model Lightcrafter 4500),<sup>‡</sup> which uses three light emitting diodes (LED) with wavelengths centered at 455 nm, 520 nm, and 630 nm as well as digital micromirror devices to modulate the light source according to the image and settings sent to the device. All images in this study were taken using the 630 nm LED. This LED's spectrum has a full width at half maximum of 17 nm with a substantially wide base. We used a 10 nm bandpass filter centered at 633 nm to further narrow the spectral width and to eliminate that base. The illumination is approximately 20° from the sample surface normal. The DLP has 1140 pixels × 912 pixels arranged in a diamond pattern [see Fig. 1(b)]. Each pixel is pulse-width modulated to achieve a projected light level. The frame period of the projector is 8.33 ms. Sinusoidal intensity patterns were used to create the structured illumination. Seven different spatial frequencies,  $f = (0, 0.12, 0.17, 0.25, 0.33, 0.50, 1.0) \text{ mm}^{-1}$  (corresponding to periods of  $\infty, 24, 18, 12, 9, 6,$  and  $3$  pixels on the projector, respectively), each with six different phases  $\varphi$  were used for the experiment, where  $\varphi = (0^\circ, 60^\circ, 120^\circ, 180^\circ, 240^\circ, 300^\circ)$ . While only three phases are required,<sup>14</sup> six were used here to oversample the results. Spatial frequencies that are not commensurate with the pixel pattern create artifacts in the data, and care was taken to avoid them. The projected sinusoidal pattern can also be displayed in both horizontal and vertical directions, both of which are used in this manuscript.

---

<sup>‡</sup>Certain commercial equipment, instruments, or materials are identified in this paper in order to specify the experimental procedure adequately. Such identification is not intended to imply recommendation or endorsement by the National Institute of Standards and Technology, nor is it intended to imply that the materials or equipment identified are necessarily the best available for the purpose.

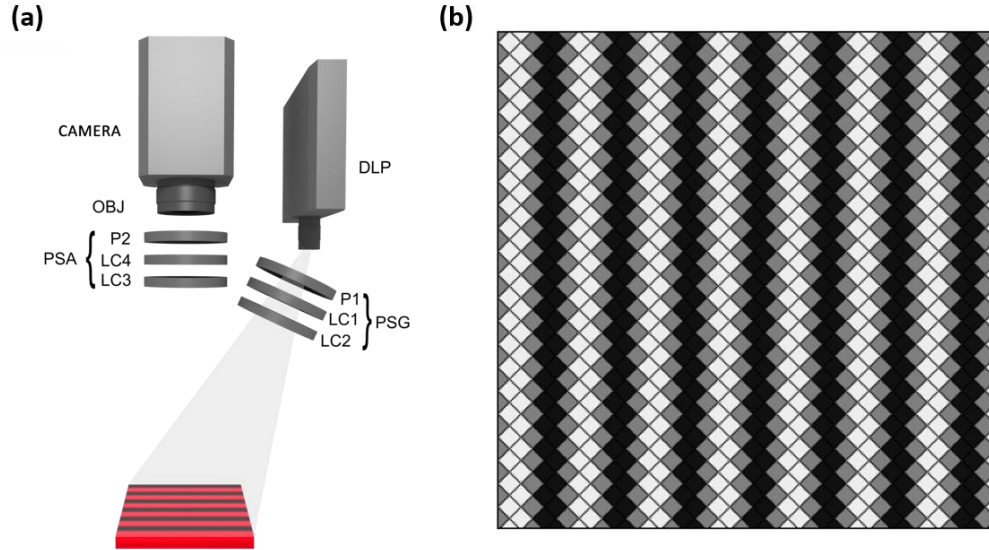


**Figure 1** (a) MMP-SFDI system: polarization state generator (PSG) with polarizer (P1) and two liquid crystal retarders (LC1 and LC2), digital light processing projector (DLP), polarization state analyzer (PSA) with polarizer (P2) and two liquid crystal retarders (LC3 and LC4), objective (OBJ), sCMOS camera (CAMERA). (b) A representation of how the sinusoid pattern for  $f = 0.5 \text{ mm}^{-1}$  is displayed by the DLP projector pixels.

The sample is imaged normal to the sample with a 50 mm focal length objective (Edmund Optics, model 59-873) onto a 16-bit  $2048 \times 2048$  scientific complementary metal oxide semiconductor (sCMOS) camera with  $(6.5 \times 6.5) \mu\text{m}^2$  pixel area (PCO, model pco.panda 4.2). The system has a full field of view (FOV) at the sample plane of  $7.5 \text{ cm} \times 7.5 \text{ cm}$ , though all images presented here are cropped to  $300 \text{ pixels} \times 300 \text{ pixels}$  and  $1.1 \text{ cm} \times 1.1 \text{ cm}$ . The camera is synchronized to the projector, and its exposure time is set as a multiple number of milliseconds. Thus, in order to avoid interference of the camera exposure time with the pulse width modulation of the projector, the camera exposure time must be a multiple of 50 ms ( $6 \times$  the frame period of the projector).

The polarization state generator (PSG) and the polarization state analyzer (PSA) each consist of a polarizer and a pair of nematic liquid crystal retarders (LC) (Meadowlark Optics). The axes of the LCs are aligned nominally at  $27.4^\circ$  and  $72.4^\circ$  with respect to the polarizer, which is the optimum configuration.<sup>15</sup> Each of the four LCs had two retardance (applied voltage) states allowing for the 16 different possible combinations needed to create a full Mueller matrix. The MMP was calibrated with the eigenvalue method described by Compain *et al.* using three samples<sup>16</sup>: air (no sample, in transmittance), a Glan-Thompson polarizer (in transmittance), and a Si wafer with an approximately 1000 nm thick  $\text{SiO}_2$  layer acting as a mirror with retardance and diattenuation (in reflection with an incident angle of  $60^\circ$ ). The 10 nm spectral bandwidth filter, mentioned earlier, was found to be necessary in order to achieve an acceptable calibration. Control of the projector, the LCs, and the camera was performed using a script written in MATLAB (Mathworks) software.

The final array of 672 images ( $7 \text{ spatial frequencies} \times 6 \text{ phases} \times 16 \text{ PSG/PSA combinations}$ ) took an acquisition time of 7.5 min if only imaged with one spatial frequency orientation. This was significantly improved from the previous iteration of the instrument, mostly due to the use of a faster camera.<sup>13</sup> The limiting factor to acquisition time comes from the response and settling time of the liquid crystal retarders. The use of a faster camera necessitated synchronizing the camera to the projector and ensuring that the camera exposure time was appropriate for the projector frame rate.

## 2.2 Analysis

Due to the combined nature of our SFDI-MMP imaging system the data array must first be demodulated before the Mueller matrices can be analyzed. Demodulation is the process by which the six phases used to modulate each spatial frequency are combined to create a single dataset for each spatial frequency containing the amplitude of modulation.<sup>10</sup> There are 16 images for each spatial frequency corresponding to the polarization states generated and

analyzed by the PSG and PSA, respectively. These sets of 16 images are used to create a Mueller matrix for each spatial frequency using the MMP reduction matrix determined from the calibration.

Each Mueller matrix was analyzed using the Lu-Chipman decomposition.<sup>17</sup> This method allows for a Mueller matrix to be decomposed into three constituent matrices representing the polarization properties of depolarization, retardance, and diattenuation. The diattenuation and depolarization data shown in this paper is on a scale from 0 to 1. A diattenuation  $D = 0$  indicates that there is no selectivity of polarized light transmittance, while  $D = 1$  indicates one polarization state is entirely attenuated. In the case of depolarization  $\Delta = 0$  indicates no depolarization, while  $\Delta = 1$  is totally depolarizing.

### 2.3 Samples

Images were acquired with polydimethylsiloxane (PDMS) (Corning, model Sylgard 184 Elastomer) scattering and absorbing phantoms acting as diffusive layers that could be added over another sample to simulate depth. Titanium dioxide ( $\text{TiO}_2$ , Atlantic Equipment Engineers, Inc.) and carbon black particles (Glassy carbon spherical powder, Alfa Aesar) embedded within the PDMS act as scatterers and absorbers, respectively. The phantoms were prepared by the protocol described elsewhere.<sup>18</sup> The PDMS phantoms varied by three different values of  $\text{TiO}_2$  mass fraction (0.05 %, 0.10 %, and 0.15 %) across two different carbon black mass fractions (0.0020 % and 0.0025 %). These PDMS phantoms were imaged individually and layered incrementally over a laser-printed National Institute of Standards and Technology (NIST) logo.

We also chose to image fiber bundles (image conduit), because they are anisotropic scatterers and may exhibit some form birefringence or diattenuation. We imaged three different fiber bundles and show the results from one of them. The fiber bundle we show had a diameter of 3.2 mm, contained 50 419 individual fibers having 12  $\mu\text{m}$  cores, and was approximately 25 mm long (Edmund Optics, model 53-839). We imaged the fiber bundles on a black felt background and on a white sintered polytetrafluoroethylene (PTFE) reflectance standard background. We only show the results for the white background.

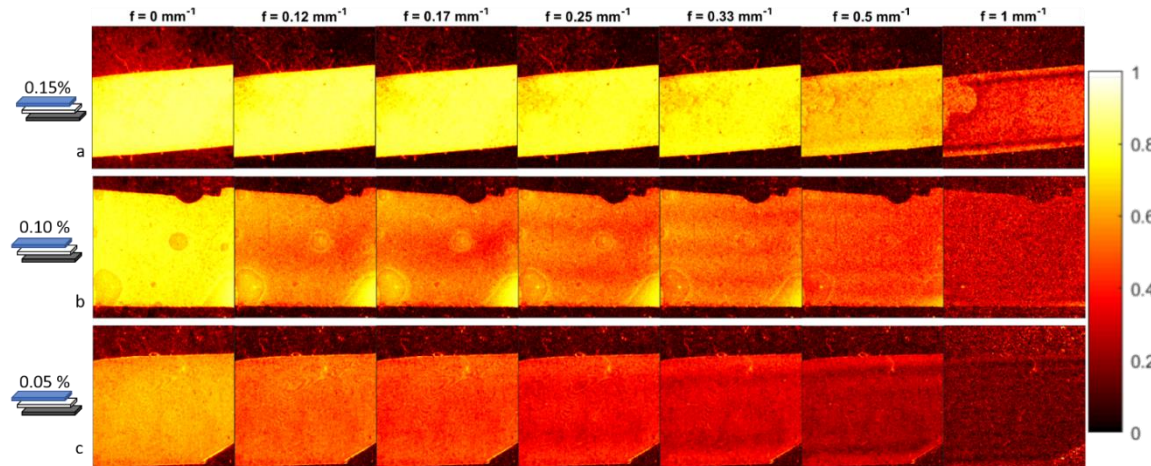


**Figure 2** Depolarization images of PDMS-based absorbing and scattering phantoms laid on a glass slide with a black felt background. The headings of the columns are the spatial frequency of the projected pattern. All three rows have the same carbon black mass fraction of 0.0025 %. The  $\text{TiO}_2$  mass fractions of rows a, b, and c are 0.15 %, 0.10 %, and 0.05 %, respectively. The color scale shows the depolarization.

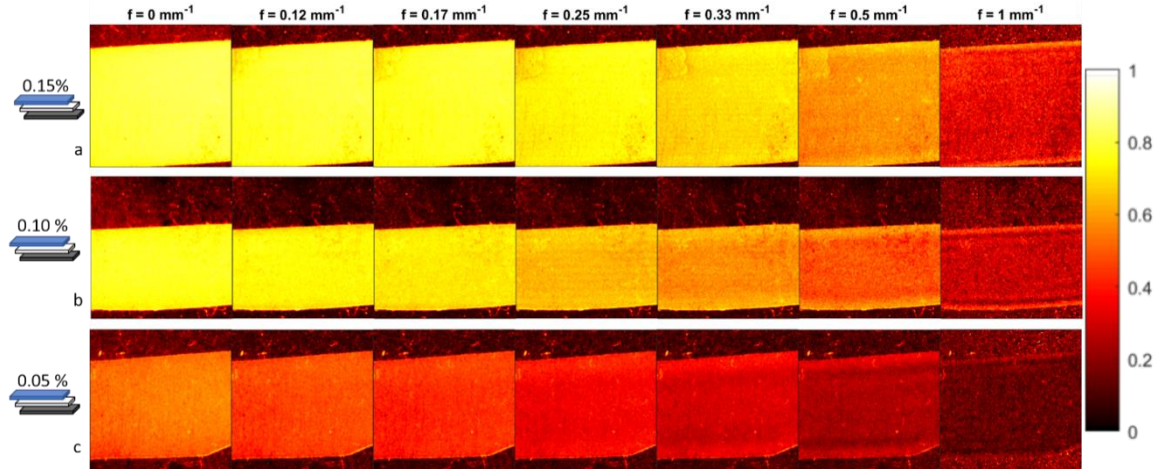


**Figure 3** Depolarization images of PDMS-based absorbing and scattering phantoms laid on a glass slide with a black felt background. The headings of the columns are the spatial frequency of the projected pattern. All three rows have the same carbon black mass fraction of 0.0020 %. The TiO<sub>2</sub> mass fractions of rows a, b, and c are 0.15 %, 0.10 %, and 0.05 %, respectively. The color scale shows the depolarization.

Figure 3 shows similar depolarization images, similar to those of Fig. 2, but with lower carbon black mass fraction (0.0020 %). Depolarization decreases more quickly as spatial frequency increases. There's significantly less depolarization between the two figures for the phantom with the least scattering.

### 3 Results and Discussion

#### 3.1 PDMS-based scattering and absorbing phantom

We investigated depolarization, retardance, and diattenuation images for the different PDMS phantoms as a function of the illumination spatial frequency. Figure 2 shows the results for depolarization for the phantoms containing a constant carbon black mass fraction and three different TiO<sub>2</sub> mass fractions. These phantoms were laid on a glass microscope slide with a black felt background.

The results show that the individual phantoms displayed an increase in depolarization as the phantoms increased in scattering for each spatial frequency. For each of the samples, as the spatial frequency increases the depolarization decreases. This decrease in depolarization is anticipated as higher spatial frequencies mask multiply-scattered light. That is, photon paths that are longer than the illumination period do not contribute to modulations as the phase is varied and thus do not contribute to the signal. The depolarization images for the sample with 0.10 % TiO<sub>2</sub> mass fraction [Fig. 2(b)] show artifacts that result from air pockets between the PDMS and the glass slide. These artifacts are reduced or removed as the spatial frequency increases, especially beyond 0.5 mm<sup>-1</sup>, suggesting that the higher spatial frequencies do not probe as deep into the material.

Figure 4 displays depolarization as a function of spatial frequency the images in Fig. 2. The error bars were calculated by taking the standard deviation of each averaged 60 pixels x 60 pixels subsection. There is around a 0.20 difference in starting depolarization between 0.15 % and 0.05 % mass fraction scattering phantoms in the plot, and the depolarization gradually decreases as spatial frequency increases due to the shortening of photon probing length. The weaker scattering profile of the 0.05 % phantom causes it to have lower maximum and minimum depolarization.

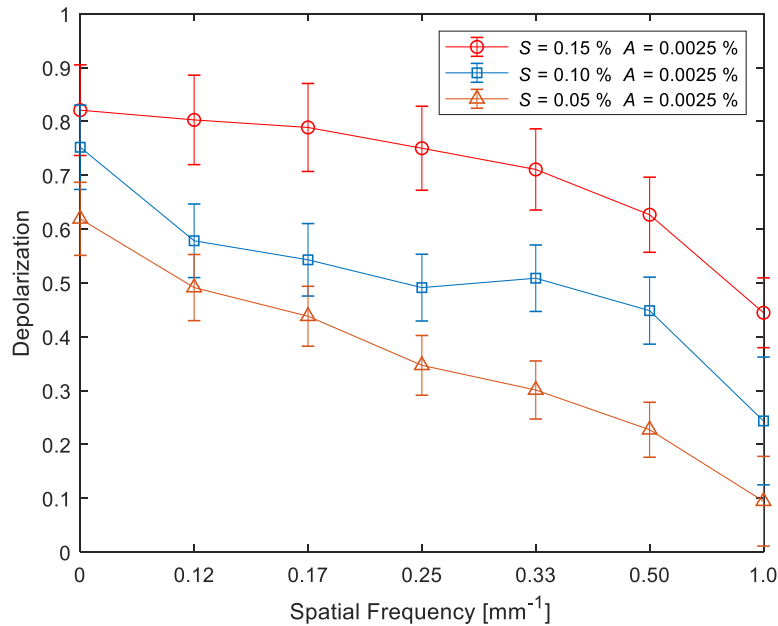


**Figure 4** Comparison of depolarization of PDMS phantoms with varying TiO<sub>2</sub> mass fractions in Figure 2. The scatterplot points are averaged over 60 pixels by 60 pixels subsections and the standard deviations are indicated. In the legend, *S* indicates TiO<sub>2</sub> mass fraction, and *A* indicates carbon black mass fraction.

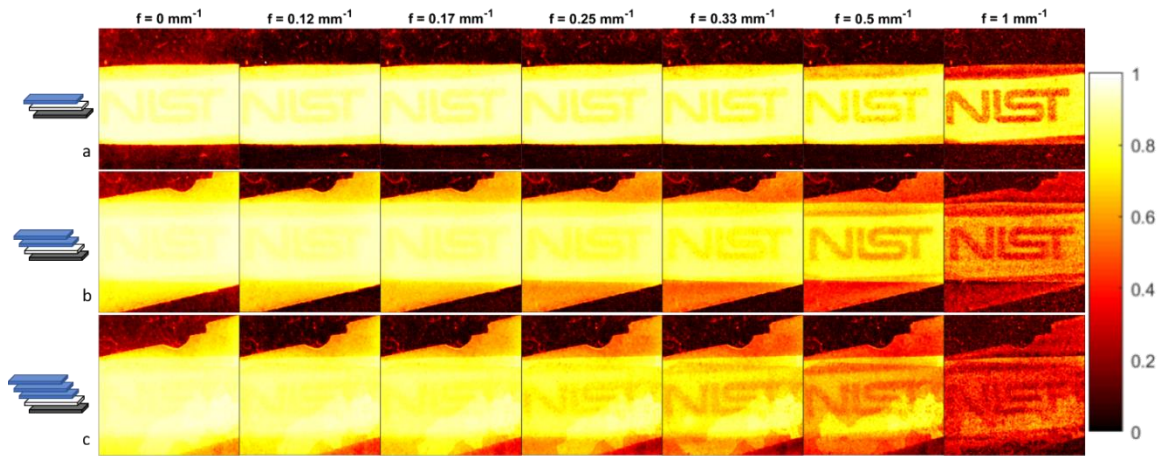


**Figure 5** Depolarization images of layers of PDMS-based scattering and absorbing phantoms on top of a patterned absorbing background with a black felt background. The headings of the columns are the spatial frequency of the projected pattern. Row a has only the 0.15 % TiO<sub>2</sub> mass fraction phantom. Row b has the 0.15 % and 0.10 % TiO<sub>2</sub> mass fraction phantoms layered above the logo. Row c has all three phantoms layered on the logo. The color scale shows the depolarization.

### 3.2 PDMS phantom layered over a patterned background

In this section, we describe measurements where we layered the 0.0025 % carbon black mass fraction phantoms on top of an absorption-modulated background (black laser-printed toner on paper). In these measurements, there is no glass slide, and there is black felt behind the paper. Figure 5 shows depolarization for (a) the 0.15 % TiO<sub>2</sub> mass fraction phantom, (b) the 0.15 % and 0.10 % TiO<sub>2</sub> mass fraction phantoms, and (c) the 0.15 %, 0.10 %, and 0.05 % TiO<sub>2</sub> mass fraction phantoms. In all the images in Fig. 5, there is less depolarization in the regions above the printing, because the absorbing logo reduces the scattering length. As spatial frequency is increased, the contrast of the logo

first increases. As the thickness increases, the spatial frequency for comparable image contrast shifts to smaller spatial frequency. For the thickest layer and the highest spatial frequency, the contrast in the image is very poor.

### 3.3 Optical fiber bundle

Figures 6 and 7 show depolarization and diattenuation images, respectively, taken of the optical fiber bundle. The images were taken for the bundle oriented vertically and horizontally, as well as for the sinusoidal illumination aligned along the fiber and perpendicular to it. The background is a highly reflective and depolarizing sintered PTFE material commonly used as a reflectance standard. This bundle is expected to exhibit much greater scattering perpendicular to the fibers. In addition, it is expected to exhibit form birefringence. Thus, the results for depolarization and diattenuation depend upon the orientation of the illuminating spatial frequency. When the sinusoidal illumination lines are aligned along the bundle [as in Fig. 6(a) and (d) and Fig. 7(a) and (d)], the measurement is probing light scattered perpendicular to the fiber, while the opposite is true when the sinusoidal illumination lines are aligned perpendicular to the bundle [as in Fig. 6(b) and (c) and Fig. 7(b) and (c)]. The scattering length in the former case is much shorter. In Fig. 6(a) and (d), the depolarization reduces significantly, even for the lowest non-zero spatial frequency,  $f = 0.12 \text{ mm}^{-1}$ . On the other hand, in Fig. 6(b), the depolarization contrast is weak, even for  $f = 0.5 \text{ mm}^{-1}$ . The differences between depolarization images of the vertically and horizontally aligned bundles is a result of the different optical geometry; the light is incident in all cases  $20^\circ$  from the left side of the image. Similar behaviors can be observed in the diattenuation images shown in Fig. 7. Interestingly, different features in the fiber bundle are observed at different spatial frequencies. That is, there is not necessarily monotonic behavior as the spatial frequency is increased. For example, the diattenuation is particularly strong in the fiber image in Fig. 7(d) for  $f = 0.25 \text{ mm}^{-1}$ . Some resonance may be occurring when the spatial frequency is comparable to the width of the bundle.

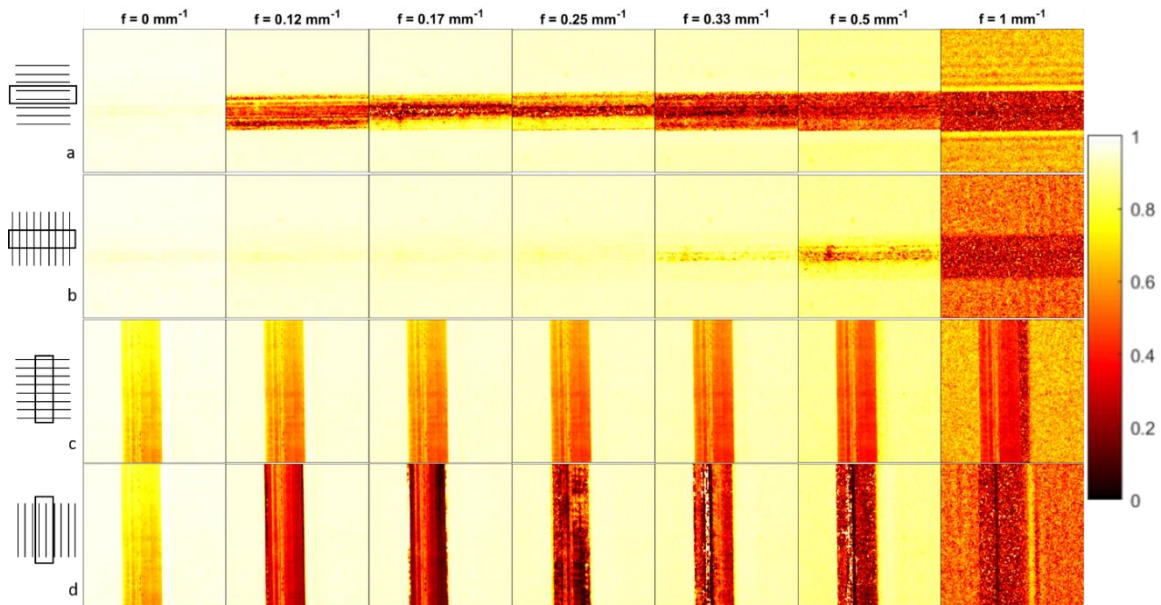


**Figure 6** Depolarization images of a bundle of  $12 \mu\text{m}$  diameter optical fibers on a white sintered PTFE reflectance standard background. The headings of the columns are the spatial frequency of the projected pattern. The rows show (a) horizontal fiber with horizontal sinusoidal pattern, (b) horizontal fiber with vertical sinusoidal pattern, (c) vertical fiber with horizontal sinusoidal pattern, (d) vertical fiber with vertical sinusoidal pattern. The color scale shows the depolarization.

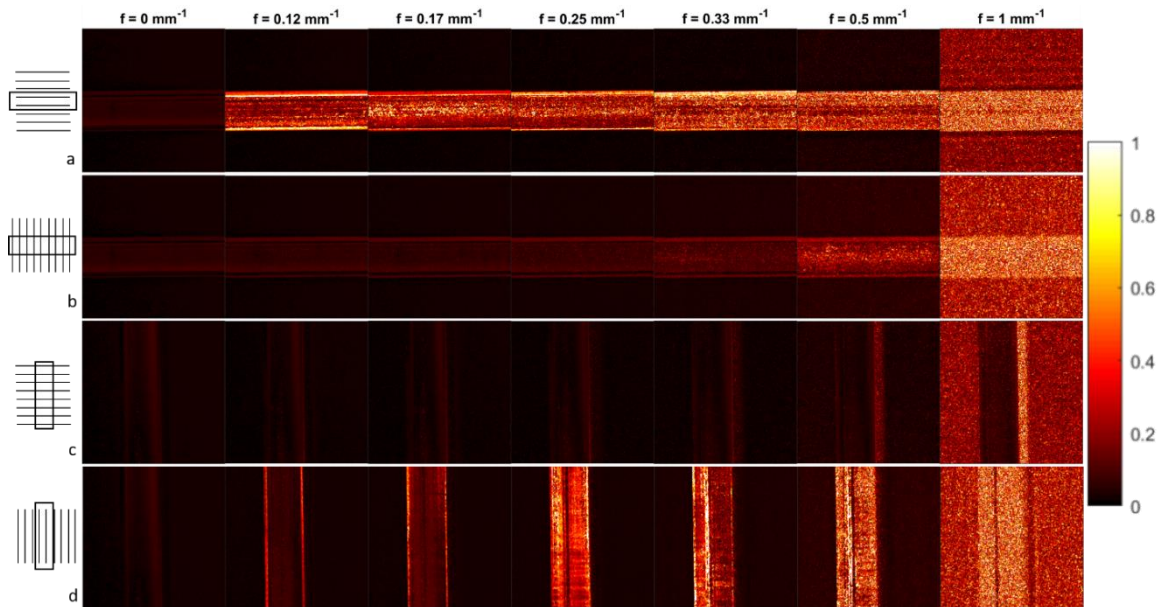


**Figure 7** Diattenuation images of a bundle of 12  $\mu\text{m}$  diameter optical fibers on a white sintered PTFE reflectance standard background. The headings of the columns are the spatial frequency of the projected pattern. The rows show (a) horizontal fiber with horizontal sinusoidal pattern, (b) horizontal fiber with vertical sinusoidal pattern, (c) vertical fiber with horizontal sinusoidal pattern, and (d) vertical fiber with vertical sinusoidal pattern. The color scale shows the diattenuation.

## 4 Summary

We demonstrate an imaging modality that combines Mueller matrix polarimetry with spatial frequency imaging. While this measurement method is very much in its infancy, we show that it has potential for distinguishing the polarization behavior for different photon path lengths in a material. In addition, we observe a dependence of the depolarization and diattenuation images on the orientation of the illumination spatial frequency for a highly anisotropic material, showing that the polarization response can be dependent upon the direction a photon path takes. Future work will continue to explore the utility of this imaging method for biomedical applications.

## References

- [1] A. Pierangelo et al., "Multispectral Mueller polarimetric imaging detecting residual cancer and cancer regression after neoadjuvant treatment for colorectal carcinomas," *J. Biomed. Opt.* **18**(4), 046014 (2013).
- [2] N. Ghosh, M. F. Wood, and I. A. Vitkin, "Mueller matrix decomposition for extraction of individual polarization parameters from complex turbid media exhibiting multiple scattering, optical activity, and linear birefringence," *J. Biomed. Opt.* **13**(4), 044036 (2008).
- [3] G. Jarry et al., "Coherence and polarization of light propagating through scattering media and biological tissues," *Appl. Opt.* **37**(31), 7357-7367 (1998).
- [4] J. Vizet et al., "In vivo imaging of uterine cervix with a Mueller polarimetric colposcope," *Sci. Reports* **7**(1), 2471 (2017).
- [5] J. Chue-Sang et al., "Use of Mueller matrix colposcopy in the characterization of cervical collagen anisotropy," *J. of Biomed. Opt.* **23**(12), 121605 (2018).
- [6] W. Sparks et al., "Spectropolarimetry of primitive phototrophs as global surface biosignatures," *Astrobiology* **21**, 219-234 (2020).
- [7] C. H. L. Patty et al., "Imaging linear and circular polarization features in leaves with complete Mueller matrix polarimetry," *Biochimica et Biophysica Acta (BBA) - General Subjects* **1862**(6), 1350-1363 (2018).
- [8] W. B. Sparks et al., "Detection of circular polarization in light scattered from photosynthetic microbes," *Proc. Nat. Acad. Sci.* **106**(19), 7816-7821 (2009).

- [9] J. M. Bueno et al., "Enhancement of confocal microscopy images using Mueller-matrix polarimetry," *J. Microscopy* **235**(1), 84-93 (2009).
- [10] J. Angelo et al., "Review of structured light in diffuse optical imaging," *J. Biomed. Opt.* **24**(7), 071602 (2018).
- [11] S. Gioux, A. Mazhar, and D. J. Cuccia, "Spatial frequency domain imaging in 2019: principles, applications, and perspectives," *J. Biomed. Opt.* **24**(7), 071613 (2019).
- [12] B. Yang et al., "Polarized light spatial frequency domain imaging for non-destructive quantification of soft tissue fibrous structures," *Biomed. Opt. Express* **6**(4), 1520-1533 (2015).
- [13] J. P. Angelo, T. A. Germer, and M. Litorja, "Structured illumination Mueller matrix imaging," *Biomed. Opt. Express* **10**(6), 2861-2868 (2019).
- [14] D. J. Cuccia et al., "Quantitation and mapping of tissue optical properties using modulated imaging," *J. Biomed. Opt.* **14**(2), 024012 (2009).
- [15] B. Laude-Boulesteix et al., "Mueller polarimetric imaging system with liquid crystals," *Appl. Opt.* **43**(14), 2824-2832 (2004).
- [16] E. Compain, S. Poirier, and B. Drevillon, "General and self-consistent method for the calibration of polarization modulators, polarimeters, and Mueller-matrix ellipsometers," *Appl. Opt.* **38**(16), 3490-3502 (1999).
- [17] S.-Y. Lu, and R. A. Chipman, "Interpretation of Mueller matrices based on polar decomposition," *J. Opt. Soc. Am. A* **13**(5), 1106-1113 (1996).
- [18] J. Hwang et al., "Polydimethylsiloxane tissue-mimicking phantoms for quantitative optical medical imaging standards," *Proc. SPIE* **10056**, 1005603 (2017).